

Contribution of Anthropogenic Activities to the Intensification of Heat Index-based Spatiotemporally Contiguous Heatwave Events in China

Dongdong Kong^{1,2}, Yuxuan Xie¹, Xihui Gu^{1,2*}, Louise Slater³, Hui Ci⁴, Heyang Song¹

Surnames or family names are underlined.

1. Department of Atmospheric Science, School of Environmental Studies, China University
of Geosciences, Wuhan, China;

2. Centre for Severe Weather and Climate and Hydrogeological Hazards, 430074 Wuhan,
China;

3. School of Geography and the Environment, University of Oxford, Oxford OX1 3QY, UK;

4. School of Geographical Sciences, Jiangsu Second Normal University, Nanjing 211200,
China

* Corresponding authors: Xihui Gu (guxihui421@163.com)

For: Journal of Geophysical Research: Atmospheres

Date of resubmission: 31 Dec 2023

Abstract In this study, we identified heat index (HI)-based spatiotemporally contiguous heatwaves (HI-STHWs) in China based on meteorological observations and CMIP6 global climate model simulations. We analyzed the spatiotemporal patterns of changes in HI-STHWs in the past and future and quantitatively attributed these changes to anthropogenic activities. The results show that the duration, severity, average, maximum, and total impacted area of the annual strongest HI-STHWs during the present period of 1991–2014 are 1.77, 2.0, 1.05, 1.14, and 1.89 times the historical period of 1961–1990, respectively. In the fingerprint results, the anthropogenic greenhouse gases (GHG) signal is significantly detected, while the aerosol (AER) and natural (NAT) signals are not. GHG is the primary factor driving the intensification of HI-STHWs, which alone explains about 130%, 122%, 112%, 111%, and 114% of the above changes. The reason for GHG contribution exceeding 100% is that AER might have a negative contribution although nonsignificant. In the future warming climate, anthropogenic activities are projected to lead to more unprecedented HI-STHWs. Under the high emissions scenario of SSP585, by 2100, the annual strongest HI-STHW in China is projected to last almost the whole year and influence 96% regions of China in the most serious day. Meanwhile, its duration and total impacted area are 24.5 [17.2, 31.6] (90% confidence interval) and 107.2 [70, 129.9] times the preindustrial period. However, if the warming level could be limited to 2/1.5 °C, those values would be 3.4/5.4 and 8.2/16.2 times smaller than that under the SSP585 scenario by 2100.

Keywords: Heat index; Spatiotemporally contiguous heatwaves; Anthropogenic activities; Anthropogenic attribution; China

Plain Language Summary

Heatwaves (HWs) are spatiotemporally contiguous events. However, previous studies often ignored the spatiotemporally contiguous property of HWs. In this study, we identified heat index (HI)-based spatiotemporally contiguous heatwaves (HI-STHWs) in China using a modern spatiotemporal clustering algorithm. We analyzed the spatiotemporal patterns of changes in HI-STHWs in the past and future and investigated the behind reasons. From 1961 to 2014, the duration, severity, average, maximum, and total impacted area of the annual strongest HI-STHWs increased significantly. Attribution analysis results show that anthropogenic greenhouse gases are the primary factor driving the intensification of HI-STHWs. In the future warming climate, more unprecedented and deadly HI-STHWs will occur. Under the business-as-usual developing scenario, by 2100, the total impacted area of the annual strongest HI-STHWs will be 206.2 times that in the preindustrial period. However, if the warming level could be limited to 2/1.5 °C, this value is 8.2/16.2 times smaller. Our findings call for urgent action to cut greenhouse gas emissions and control the warming level, which can reduce the impact of HI-STHWs efficiently.

Key Points

- GHG is the primary factor driving the intensification of heat index-based spatiotemporally contiguous heatwave events (HI-STHWs)
- Under the SSP585 scenario, HWD and HWA_{sum} are 24.5 [17.2, 31.6] and 107.2 [70, 129.9] times the preindustrial period
- If the warming level could be limited to 2/1.5 °C, HWA_{sum} would be 8.2/16.2 times smaller than that under the SSP585 scenario by 2100

1. Introduction

Heatwaves (HWs) are typically defined as periods in which the near-surface air temperature (T) exceeds a certain threshold for no less than three days (Perkins, 2015; You et al., 2017). HWs can pose severe threats to many aspects of society and ecosystems, such as public health (McMichael et al., 2006; Zhang et al., 2023), crop production (Yuan et al., 2016), energy supply (Larcom et al., 2019), and ecosystem security (Frölicher et al., 2018a). Compared with T -based HWs, heat index (HI)-based HWs are more closely related to human-perceived heat, morbidity and mortality (Fischer & Knutti, 2013; Kong et al., 2020; C. Li et al., 2020; J. Li et al., 2018; Mora et al., 2017; Russo et al., 2017), as the HI additionally considers the influence of relative humidity (RH) on the body's ability to cool itself through perspiration (Rothfusz & Headquarters, 1990).

Heatwaves (HWs) are spatiotemporally contiguous events. However, many studies have analyzed HW characteristics only at the station or grid point level, often ignoring the fact that HWs are spatiotemporally contiguous events. HWs can be vast in space and last for a long period. For example, the 2013 summer HW event in central and eastern China lasted for more than 30 days (S. Ma et al., 2017; Sun et al., 2014) and covered most regions of the Yangtze River basin. The 2015 summer HW in western China lasted for approximately 60 days and covered an area of approximately 753,000 km² (Sun, Song, et al., 2016). HWs can also migrate from one region to another and merge or split over time during their development and conclusion. Taking the 2013 summer HW as an example (Fig. S5), on August 6, the HW originated in the northern region of China. By August 12, the intensity of the heatwave escalated in Qinghai and Tibet, eventually merging into a unified HW that collectively baked the Yangtze River Basin. After August 18, it entered a declining phase, with the HW's influence shifting westward and gradually diminishing.

Understanding the changing characteristics of spatiotemporally contiguous heatwaves (STHWs) can provide new insight into how HWs will change under a warming climate. Some researchers have paid attention to changes in STHWs in the past and future. Lo et al. (2021) developed an objective spatial and temporal connectivity algorithm to track STHWs over global terrestrial areas during 1979–2018 based on reanalysis data. From a regional perspective, Luo et al. (2022a) indicated that China experienced more frequent, intenser, longer-lasting, and more widespread STHWs during 1961–2018. (Keellings & Moradkhani, 2020) found a considerable increase in a spatial metric combining the frequency, magnitude, duration, and areal extent of STHWs in the United States during 1981–2018. In addition to these historical changes in STHWs, Lyon et al. (2019) projected an increase in the areal extent of STHWs in the United States under future warming. Vogel et al. (2020) also projected more frequent STHWs globally and pointed out that thermodynamic factors strongly contribute to the increase in global climate model (GCM)-simulated STHWs. However, these studies mainly focused on T -based STHWs. Although HI -based STHWs (abbreviated HI-STHWs hereafter) provide a better characterization of HWs as felt by humans, there is still limited understanding of the past occurrences and future changes of HI-STHWs. Previous studies have indicated with high confidence that global warming is accompanied by a strong reduction in RH (Fischer & Knutti, 2013), and the joint impact of RH reduction and warming will lead to more unprecedented HWs (Dunne et al., 2013). Hence, the analysis of HI -STHWs is likely to provide different findings relative to the analysis of T -based STHWs.

Detection and attribution techniques have become increasingly mature in the past two decades (Allen & Stott, 2003; Y. Li et al., 2021; Ribes & Terray, 2013). The signal of anthropogenic activities has been significantly detected in the increase in HWs (Christidis et al., 2015; Kong et al., 2020; C. Li et al., 2020; Seong et al., 2021; Stott et al., 2004; Sun et al., 2014) during the last few decades based on optimal fingerprint methods (Allen & Stott, 2003;

Ribes & Terray, 2013). However, to our knowledge, all HW detection and attribution analyses have focused on traditional HW characteristics at the station or grid point level, and corresponding analyses of STHWs from a three-dimensional (3D) perspective are still lacking. Although previous studies have revealed increases in the areal extent and frequency of STHWs in the historical warming climate, suggesting that these increases may be driven by global warming (Luo et al., 2022a; Lyon et al., 2019), there is no quantitative evidence supporting whether the signal of anthropogenic activities can be detected in the changes in STHWs.

In this study, we identify HI-STHWs in China using a modern spatiotemporal clustering algorithm. Then, we address the following questions:

- What are the changes in the characteristics of HI-STHWs in China in the past and future?
- Is there a signal of anthropogenic emissions in the historical changes in the characteristics of HI-STHWs?
- If so, what is the relative contribution of anthropogenic activities to these changes?

To answer these questions, (1) we investigate the patterns of changes in HI-STHW characteristics in the historical period; (2) employ the regularised optimal fingerprint method (Ribes & Terray, 2013) to detect anthropogenic signals and attribute anthropogenic contributions based on meteorological observations and the Coupled Model Intercomparison Project Phase 6 (CMIP6) GCM-simulated HI-STHWs; and (3) finally present the future evolution of HI-STHWs under two representative shared socioeconomic pathways (SSPs), SSP126 and SSP585 (Fig. 1). This study seeks to help understand the anthropogenic contribution to increases in HI-STHWs and the future evolution and spatiotemporal characteristics of HI-STHWs under different development paths and warming levels in the future warming climate.

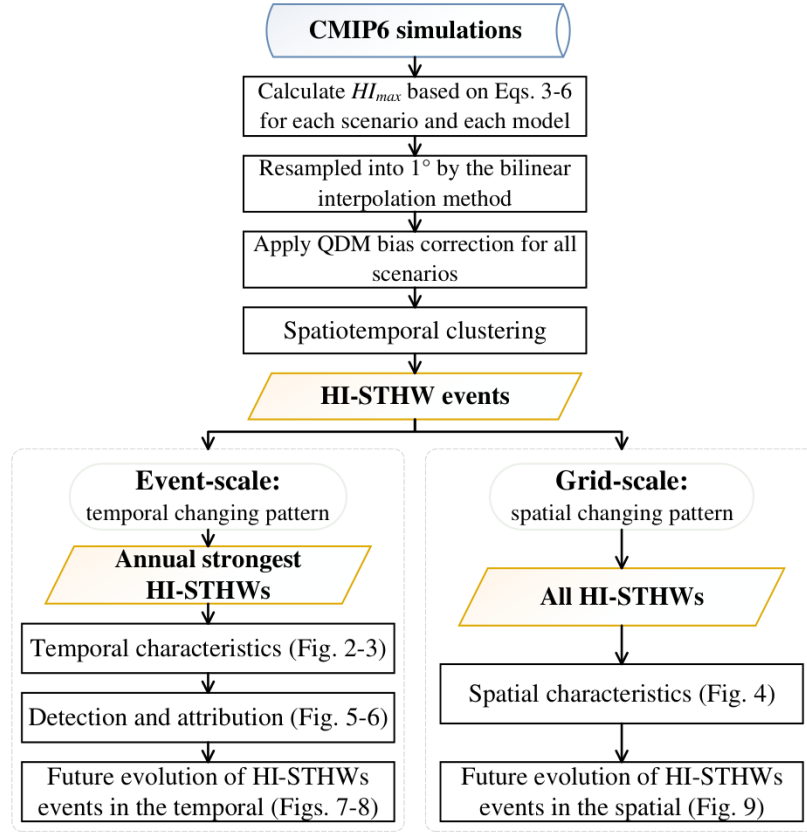


Fig. 1. The framework of this study. Details of temporal and spatial characteristic indexes can be found in Table 2.

2. Data and Methods

2.1 Data

2.1.1 Observed gridded daily meteorological data

In this study, the daily maximum heat index (HI_{max}) was used to identify HI-STHW events. Usually, HI_{max} is corresponding to the daily maximum air temperature (T_{max}) and the daily minimum relative humidity (RH_{min}). T_{max} and RH_{min} are used to calculate HI_{max} (section 2.2). But for the observed meteorological data, we only have the daily T_{max} and daily mean relative humidity (RH_{mean}). Fig. S2 shows that daily RH_{mean} derived HI_{max} has a substantial positive bias, especially for the summer and Southern humid region (e.g., Guangzhou), which indicates that we can't use the daily RH_{mean} and T_{max} directly for the calculation of HI_{max} . Compared with air temperature strongly influenced RH , q , as well as actual vapor pressure (e_a), can be regarded as a constant within a day (Fig. S1). By assuming

q and e_a as constant, daily RH_{min} can be derived by daily mean air temperature (T_{mean}), T_{max} , and RH_{mean} (Eqs. 1-2). Although this assumption cannot be strictly satisfied, it has already significantly reduced the errors of HI_{max} calculation (see details in supplementary Text S1 and Figs S1, S2).

$$e_s(T) = 0.6108 \exp\left(\frac{17.27T}{T + 237.3}\right) \quad (1)$$

$$e_{a,mean} = e_s(T_{mean})RH_{mean}, RH_{min} = \frac{e_{a,mean}}{e_s(T_{max})} \quad (2)$$

where $e_s(T)$ is the saturated vapor pressure (in kPa) under the air temperature T (in °C).

The observed daily T_{max} and T_{mean} were obtained from the CN05.1 dataset (Wu & Gao, 2013, <https://ccrc.iap.ac.cn/resource/detail?id=228>), which has a resolution of $0.25^\circ \times 0.25^\circ$ and covers the period 1961–2021. Previous studies have revealed that unhomogenized RH data can lead to a false decreasing trend of HI values in South China (Freychet et al., 2020; Li et al., 2020). To avoid this problem, we used the homogenized RH_{mean} from ChinaRHv1.0 dataset (Li et al., 2020), which has 746 stations on the Chinese mainland during 1960–2017. We interpolated ChinaRHv1.0 into $0.25^\circ \times 0.25^\circ$ cells using the same method as CN05.1 (Wu & Gao, 2013), namely, the thin-plate spline method and the angular distance weighting method, for climatology and anomaly interpolation, respectively. The sum of the interpolated climatology and anomaly results in the final gridded RH_{mean} dataset. For consistency with the length of CMIP6 simulations in the historical scenario, we used only T_{max} and RH_{mean} data from the period of 1961–2014.

2.1.2 Coupled Model Intercomparison Project Phase 6 (CMIP6) data

CMIP6 data is accessed at <https://esgf-node.llnl.gov/esg-search/search>. For CMIP6 GCMs data, gridded daily T_{max} and q were used to calculate HI_{max} . Their variable names in CMIP6

are *tasmax* and *huss*, respectively. Similar to the observed data, we derived RH_{min} by Eq. 3 under the same assumption that q and e_a can be regarded as a constant within a day.

$$e_a = \frac{qP_a}{0.622 + 0.378q}, RH_{min} = e_a / e_s(T_{max}), \quad (3)$$

where P_a is the air pressure, which is an insensitive variable (Fig. S3) and is treated as a constant value of 101.325 kPa here. After that, T_{max} and RH_{min} are used to calculate HI_{max} .

In the historical period (1961–2014), we used CMIP6 simulations of multiple scenarios to detect the signal of anthropogenic activities, including historical forcing (anthropogenic and natural forcings, ALL), greenhouse gas forcing only (GHG), aerosol forcing only (AER), and natural forcing only (solar and volcanic combined, NAT). Furthermore, unforced preindustrial control (*piControl*) runs were used to quantify the internal variability (Ribes et al., 2013; Ribes & Terray, 2013). In the future period (2015–2100), we used the simulations of two differing SSPs, SSP126 and SSP585, to illustrate the potential future evolution and spatial distribution of HW characteristics at different warming levels. SSP126 and SSP585 are two representative development pathways. They correspond to low-emission and high-emission development pathways, respectively, where the 2100 radiative forcing reaches 2.6 W m^{-2} and 8.5 W m^{-2} with respect to the preindustrial level (Meinshausen et al., 2020). As in previous studies (Chen & Sun, 2017; Kong et al., 2020), we used only the first ensemble of the CMIP6 simulation runs (“r1i1p1f1”) to conduct our analyses. Even though only the “r1i1p1f1” realization was used, ample simulations exist to conduct fingerprint analysis (Ribes & Terray, 2013). There are 18 *piControl* GCMs, which altogether consist of 9,396 years of simulations and 174 54-year chunks (Table 1). All CMIP6 simulations were interpolated to the same $1^\circ \times 1^\circ$ grid using the bilinear interpolation. After that, we used the delta quantile mapping (QDM) method to correct systematic biases in GCMs simulations for all scenarios (details can be found in supplementary

Text S2). The QDM method is designed to protect relative changes in quantiles, has a good performance in extreme climate events studies (Cannon, et al., 2015).

Table 1 List of GCM simulations used in this study. Here, “1” indicates that the simulations are available in the corresponding GCM; the number in the “piControl” row indicates the number of 54-year chunks in the corresponding GCM.

Model	ALL	GHG	AER	NAT	piControl	SSP126	SSP585
ACCESS-CM2	1	1	1	1	8	1	1
ACCESS-ESM1-5	1	1	1	1	18	1	1
CMCC-ESM2	1				8	1	1
E3SM-1-0	1		1		8		1
E3SM-2-0	1	1	1	1	8		
EC-Earth3	1				8	1	1
EC-Earth3-CC	1				8		1
FGOALS-f3-L	1				10		
FGOALS-g3	1	1	1	1		1	1
GFDL-CM4	1			1	8		1
GFDL-ESM4	1	1	1	1	8	1	1
IITM-ESM	1					1	
INM-CM4-8	1				8	1	1
INM-CM5-0	1				22	1	1
KIOST-ESM	1				8	1	1
MIROC6	1	1	1	1	8	1	1
MPI-ESM1-2-HAM	1				14		
MPI-ESM1-2-HR	1				8	1	1
MRI-ESM2-0	1	1	1	1	2	1	1
NorESM2-MM	1					1	1
SAM0-UNICON	1				12		
Total models	21	7	8	8	18	14	16

2.2 Detection of HI-STHWs

The extraction of HI-STHWs is based on *HI*, which is calculated using the Rothfusz regression (J. Li et al., 2018; Luo & Lau, 2018; Rothfusz & Headquarters, 1990):

$$\begin{aligned}
 HI(T, RH) = & -8.784695 + 1.61139411 \times T - 2.338549 \times RH \\
 & - 0.14611605 \times T \times RH - 1.2308094 \times 10^{-2} \times T^2 \\
 & - 1.6424828 \times 10^{-2} \times RH^2 + 2.211732 \times 10^{-3} \times T^2 \times RH \\
 & + 7.2546 \times 10^{-4} \times T \times RH^2 + 3.582 \times 10^{-6} \times T^2 \times RH^2
 \end{aligned} \quad (4)$$

where *T* is the surface air temperature (in °C) and *RH* is the relative humidity (in %),

HI(T, RH) is the function to calculate *HI* (in °C).

Eq. 4 will fail if $HI \leq 26.7^{\circ}\text{C}$ (J. Li et al., 2018; Luo & Lau, 2018; Rothfusz & Headquarters, 1990). Further adjustments should be applied when $RH < 13\%$ and $26.7^{\circ}\text{C} < T < 44.4^{\circ}\text{C}$ or $RH > 85\%$ and $26.7^{\circ}\text{C} < T < 30.6^{\circ}\text{C}$ (https://www.wpc.ncep.noaa.gov/html/heatindex_equationbody.html):

$$\begin{cases} HI = HI - \frac{(13 - RH)}{4} \times \sqrt{1 - \frac{|1.8T - 63|}{17}}, & (RH < 13\% \text{ and } 26.7^{\circ}\text{C} < T < 44.4^{\circ}\text{C}) \\ HI = HI + \frac{(RH - 85)}{10} \times (11 - 0.36T), & (RH > 85\% \text{ and } 26.7^{\circ}\text{C} < T < 30.6^{\circ}\text{C}) \end{cases}, (5)$$

It should be noted that we used daily T_{max} and RH_{min} to calculate the daily maximum HI (HI_{max} , Eq. 6).

$$HI_{max} = HI(T = T_{max}, RH = RH_{min}), \quad (6)$$

We used the spatiotemporal clustering algorithm of (Samaniego et al., 2013) (https://git.ufz.de/chs/progs/SMI/-/blob/main/src/mo_smi_drought_evaluation.f90) to detect HI-STHWs. This clustering algorithm was initially proposed to identify soil moisture droughts (Samaniego et al., 2018; Samaniego et al., 2013). It considers merging and splitting processes in the development and conclusion stages of spatiotemporal events reasonably. Compared with other spatiotemporal clustering algorithms, the method has two specific parameters $n_{connect}$ and $n_{overlap}$ to control the connected HW grids in the space and the overlapped grids over successive time steps (Fig. S4). In this method, HI-STHWs are identified by the following steps (Fig. S4):

- (1) Grids experiencing HWs are identified when the corresponding $HI \geq \text{threshold}$ (TRS). Song et al. (2022) revealed that threshold methods (e.g., the fixed threshold) that do not consider seasonal variations will weaken the continuity of HI exceedance and underestimate the increasing rate of STHW. In this study, we used a seasonally varying TRS . For each grid, on the i^{th} day of the year (doy_i , $\text{doy}_i=1, \dots, 366$), TRS_i is calculated as the 95% quantile of all HI values over a 15-day window centered over the current doy_i from

1961–1990 ($30 \times 15=450$ values). The dimensions of HI and TRS are [longitude×latitude×time] and [longitude×latitude×doy], respectively. It should be noted that HW in this study refers to HI being relatively higher with respect to the climatology, other than exceeding a fixed threshold that becomes intolerable for humans.

- (2) Spatially contiguous (edge-adjacent, 4-connected) HW grids are consolidated as one spatial HW event. Because small isolated HWs are usually unable to develop into regional and long-lasting spatiotemporal events, spatial HW events with connected HW grids of less than $n_{connect}$ are eliminated, where $n_{connect}$ equals 16 and 4 for $0.25^\circ \times 0.25^\circ$ and $0.5^\circ \times 0.5^\circ$ grids, respectively (approximately 10,000 km²) (Samaniego et al., 2013; Wei et al., 2021).
- (3) Because the spatial extent and variability of an extreme HI-STHW can be vast (Luo, et al., 2022a; F. Ma et al., 2022), different HW events can merge or split over time in the development and conclusion stages. We further consolidate spatial HW events over successive time steps as one HI-STHW. The only condition for consolidation is that the overlapped grid $\geq n_{overlap}$. For $n_{overlap}$, we use the same threshold as $n_{connect}$. The grids from the same HI-STHW event are flagged with the same HW ID ($ID = year * 1,000 + i_{HW}$, where i_{HW} represents the order of identified HI-STHW events in the current year). For example, the ID 2012,002 refers to the second HI-STHW event in 2012. For grids that are not HI-STHWs, IDs are set to -9999. Finally, IDs are stored in a 3D array *clusterID* (with the exact dimensions as the input data HI , namely, [longitude×latitude×time]).

Moreover, we rewrote the original Fortran version spatiotemporal clustering algorithm of (Samaniego et al., 2013) in the Julia language (Bezanson et al., 2017), improving its computing efficiency and reducing the memory consumed by the disjoint set algorithm (https://en.wikipedia.org/wiki/Disjoint-set_data_structure). The new Julia version is approximately 30~50 times faster. Computing HI-STHWs for one GCM with a $0.5^\circ \times 0.5^\circ$ grid and a daily scale during 1851–2014 takes only a few minutes to complete. Fig. S5 shows a case

of the observed annual strongest HI-STHW event in 2013, which can illustrates the correctness of this algorithm.

2.3 Characteristics of HI-STHWs

For each HI-STHW event, we quantified its characteristics using six indices (Table 2): HW duration (HWD), HW intensity (HWI), HW severity (HWS), average HW-impacted area (HWA_{avg}), maximum HW-impacted area (HWA_{max}) and sum of the HW-impacted area (HWA_{sum}). At the event scale, we focused only on the annual strongest HI-STHW, as indicated by the largest HWS_{sum} (Table 2 for details), to study the pattern of changes in the HI-STHW characteristics in the past and future. At the event scale, HI-STHW characteristics were spatially aggregated by grids, so only the temporal variation information was left, and spatially distributed information was lost.

We were also concerned with the spatial distribution of HI-STHW events, such as understanding where the worst HI-STHWs occur the most frequently. Hence, we further quantified HI-STHW characteristics at the grid scale to represent their spatial information using four additional indices for each grid (Table 2): HWD (duration, days impacted by HI-STHW events), HWI (intensity, maximum *HI* exceedance during HI-STHW days), HWS (severity, accumulated *HI* exceedance during HI-STHW days), and HWF (frequency, the number of HI-STHW events). These four indices were calculated in each grid cell for each year. Separately from the event-scale indices, we considered all the HI-STHW events, namely, all pixels flagged with a valid HW ID ($ID \neq -9999$), to calculate grid-scale characteristics. If we took only the annual strongest HI-STHW event into account, due to the asymmetric spatial distribution of a given HI-STHW, many regions are not impacted by a given HI-STHW; hence, no valid HW characteristics would be present in these regions.

282 **Table 2** Indices of HI-STHW characteristics at the event and grid scales. At the event scale, only the annual strongest HI-STHW is selected, where d is the HI-STHW
283 duration, the subscript i corresponds to the i th grid in space, t corresponds to the time, and t_{start} and t_{end} are the beginning and ending times of the HI-STHW. Some
284 of those indexes were borrowed from Luo et al. (2022a). At the grid scale, all HI-STHWs are included, where k corresponds to the k th HI-STHW event and n is the
285 total number of HI-STHW events that have occurred on the grid. $HI_{i,t}$ is the heat index, $TRS_{i,t}$ is the seasonally varying 95% quantile threshold, and $A_{i,t}$ is the grid
286 area. $[\]_+$ is the positive part function, $[x]_+ = \max(x, 0)$. We selected the annual strongest HI-STHW by a comprehensive index HWS_{sum} , $HWS_{sum} =$
287 $\sum_{t=t_{start}}^{t_{end}} (\sum_i A_i [HI_{i,t} - TRS_{i,t}]_+)$, which considers the intensity, duration and impacted area of HI-STHWs simultaneously.

Scale	Purpose	Index	Name	Formula	Description
Event-scale	Show the temporal characteristics of the annual strongest HI-STHW (used in Figs. 2, 3, and 5-8)	HWD	Duration (day)	$HWD = \sum_{t=t_{start}}^{t_{end}} 1$	The time interval between the beginning and ending time of HI-STHW.
		HWI	Intensity ($^{\circ}\text{C}$)	$HWI = \frac{1}{d} \sum_{t=t_{start}}^{t_{end}} \frac{\sum_i A_{i,t} [HI_{i,t} - TRS_{i,t}]_+}{\sum_i A_{i,t}}$	Mean of the daily area-weighted HI exceedance.
		HWS	Severity ($^{\circ}\text{C} \cdot \text{day}$)	$HWS = \sum_{t=t_{start}}^{t_{end}} \frac{\sum_i A_i [HI_{i,t} - TRS_{i,t}]_+}{\sum_i A_i}$	Sum of the daily area-weighted HI exceedance
		HWA_{avg}	Average of impacted area ($10^6 km^2$)	$HWA_{avg} = \sum_{t=t_{start}}^{t_{end}} \sum_i A_{i,t}$	Mean of the daily HI-STHW-impacted areas.
		HWA_{max}	Maximum of impacted area ($10^6 km^2$)	$HWA_{max} = \max_t (\sum_i A_{i,t})$	Maximum of the daily HI-STHW-impacted areas.
		HWA_{sum}	Sum of impacted area ($10^6 km^2$)	$HWA_{sum} = \sum_{t=t_{start}}^{t_{end}} \sum_i A_{i,t}$	Sum of the daily HI-STHW-impacted areas.
Grid-Scale	Show the spatial characteristics of all HI-STHWs in each year (used in Figs. 4 and 9)	HWD	Duration (day)	$HWD = \sum_{k=1}^n (\sum_{t=t_{start,k}}^{t_{end,k}} 1)$	Days with HI-STHW events.
		HWF	Frequency (times)	$HWF = \sum_{k=1}^n 1$	The number of HI-STHW events
		HWI	Intensity ($^{\circ}\text{C}$)	$HWI = \max([HI_{i,t} - TRS_{i,t}]_+)$	Maximum HI exceedance
		HWS	Severity ($^{\circ}\text{C} \cdot \text{day}$)	$HWS = \sum_{k=1}^n (\sum_{t=t_{start,k}}^{t_{end,k}} [HI_{i,t} - TRS_{i,t}]_+)$	Accumulated HI exceedance.

289 *2.4 Detection and attribution method*

290 Regularised optimal fingerprinting (ROF) is employed to detect and attribute anthropogenic
 291 contributions to the changes in HI-STHW characteristics (Ribes et al., 2013). The separate
 292 contributions of external forcing factors, i.e., ALL, GHG, AER, and NAT, are quantified. ROF
 293 is an extension of traditional ordinary least squares (Allen & Tett, 1999) and total least squares
 294 (Allen & Stott, 2003) optimal fingerprinting. ROF outperforms OLS and TLS methods in
 295 estimating the internal climate variability covariance matrix. Meanwhile, ROF does not need
 296 empirical orthogonal projections and avoids the problem of arbitrary selection of the k leading
 297 empirical orthogonal functions. ROF has been widely used to detect and attribute anthropogenic
 298 contributions to changes in extreme events, such as extreme temperature (Kim et al., 2016; Sun,
 299 Zhang, et al., 2016), extreme precipitation (Kirchmeier-Young & Zhang, 2020), and extreme
 300 Arctic sea ice extent (Kirchmeier-Young et al., 2017). Similar to TLS, ROF considers the
 301 sampling uncertainties both in the observations Y and in the simulated signals X :

$$302 \qquad Y = \sum_{i=1}^m (x_i - v_i) \beta_i + \varepsilon_0, \qquad (7)$$

$$303 \qquad C_{x_i} = \beta_i \times \text{trend}_{x_i} \times n \qquad (8)$$

304 where Y is the rank- n vector of observations, x_i is the climate model-simulated signal under the
 305 i^{th} external forcing (ALL, GHG, AER, or NAT), and β_i is the corresponding scaling factor of the
 306 signal x_i . v_i is the noise in x_i , ε_0 is the noise in Y , and m is the number of signals. A fingerprint
 307 signal is detectable if its scaling factor is positive and its 90% uncertainty range excludes zero
 308 (Y. Li et al., 2021; Ribes et al., 2013; Ribes & Terray, 2013). Interested readers can find the
 309 detailed calculation procedure of the scaling factor's uncertainty in Appendix 3 of Ribes et al.
 310 (2013). The attributable changes to external forcing can be quantified using Eq. (8), where C_{x_i} is
 311 the estimated attributable changes to external forcing x_i , trend_{x_i} is the Sen's slope trend of x_i
 312 during 1961–2014 (Kong & Song, 2022; Sen, 1968), and n is the length of the year over 1961–
 313 2014 (i.e., 54). We employed both one-signal ($m = 1$) and two-signal ($m = 2$) optimal

fingerprint analysis. The former was used to indicate whether one signal can be detected in Y ; the latter is used to indicate whether two signals (e.g., GHG and NAT) can be separated from each other (Gu et al., 2019; Kong et al., 2020; J. Liu et al., 2021).

In this study, we conducted ROF mainly based on the HI-STHW characteristics at the event scale in the historical period of 1961–2014. The input data for ROF were prepared as follows: (1) The daily T and RH of the CMIP6 GCM simulation were interpolated into $0.5^\circ \times 0.5^\circ$ grids. (2) The HI was calculated, HI-STHW events were identified, and HI-STHW temporal characteristics were evaluated at the event scale for each model and each scenario. (3) Noise data were prepared using *piControl* simulations. The *piControl* simulations from the available 18 GCMs were divided into 108-year chunks (twice the length of 1961–2014). Each of the 108-year chunks was equally divided into two parts, *noise1* and *noise2*. The former was used to estimate the covariance matrix of internal variability (namely *noise1* was regarded as v_i in Eq. 7), and the latter was used to test the residual consistency. Readers can find more details in the section 3.1 of Allen & Stott (2003). There were 9,396 years *piControl* simulations, which were finally divided into 87 54-year chunks for *noise1* and *noise2*. (4) Similar to previous studies (Gu et al., 2019; Sun, Zhang, et al., 2016), a 5-year nonoverlapping mean was applied to suppress natural internal variability for observed signal Y , simulated signals X , and *noise1* and *noise2*. Hence, the HI-STHW temporal characteristic signals from 1961–2014 were aggregated into ten 5-year nonoverlapping means and one 4-year mean (11 values in total). After this step, all inputs of the ROF (i.e., X , Y , *noise1*, and *noise2*) were prepared and ready for fingerprint analysis.

3. Results

3.1 Historical Characteristics of HI-STHW Events

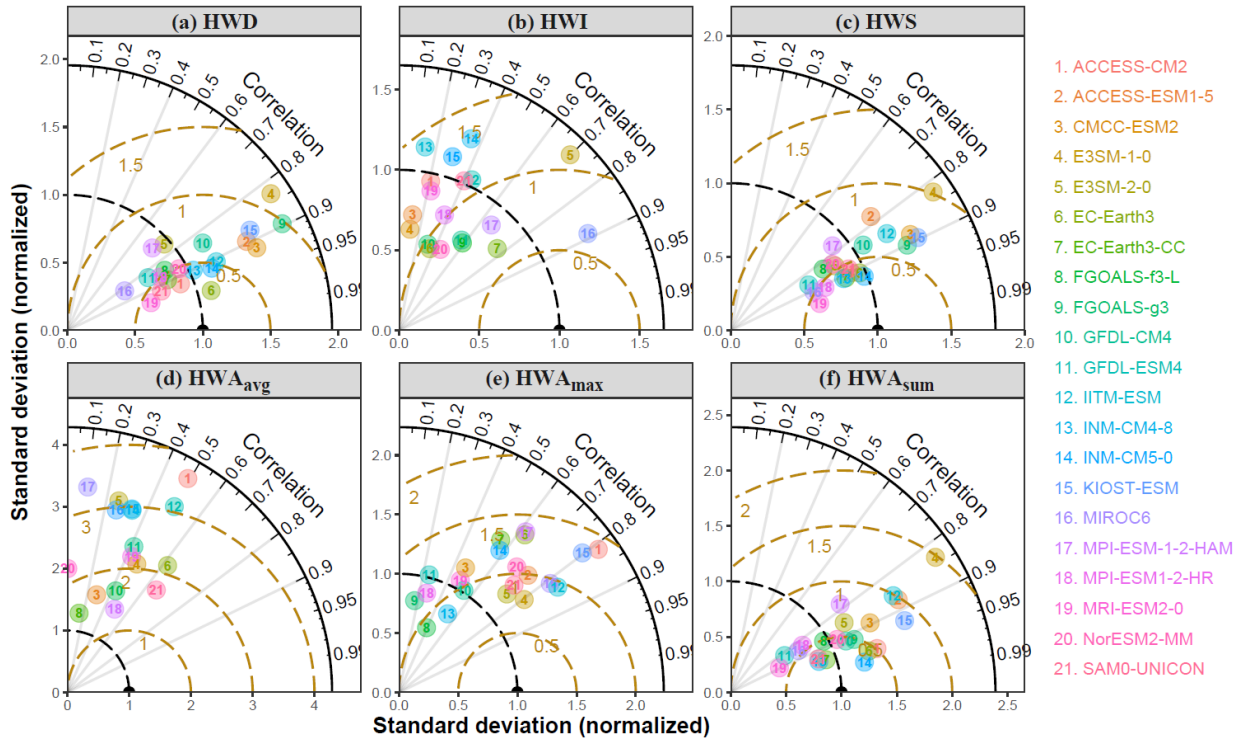


Fig. 2. Taylor diagram showing the performance of CMIP6 ALL simulations in the HI-STHW characteristics of the annual strongest HI-STHW event during 1961-2014. The brown dashed lines indicate the root mean square error (RMSE) between the observed and simulated; the grey lines indicate the Pearson correlation (R). CMIP6 simulations was bias-corrected by the QDM method. Additionally, an 11-year moving window was applied for both the observed and simulated HI-STHW characteristics to suppress interannual fluctuations caused by internal climate variability.

It can be seen from Fig. 2 that the bias-corrected CMIP6 GCMs have a good performance in most HI-STHW indexes, including HWD, HWS, HWA_{max} , HWA_{sum} , with a large number of models $R > 0.8$ and $RMSE < 1$ standard deviation of the observed. Compared with CMIP6 simulations without bias correction (Fig. S6), the R is almost the same, but the RMSE is reduced many times. Meanwhile, the performance of HWA_{avg} is weaker than HWA_{max} and HWA_{sum} , the performance of HWI is the lowest. As for HWI, because HWI has no significant trend in the last decades (Fig. 3), HWI is not the key point of our study, hence the lower performance of HWI has very limited impact in the subsequent analysis.

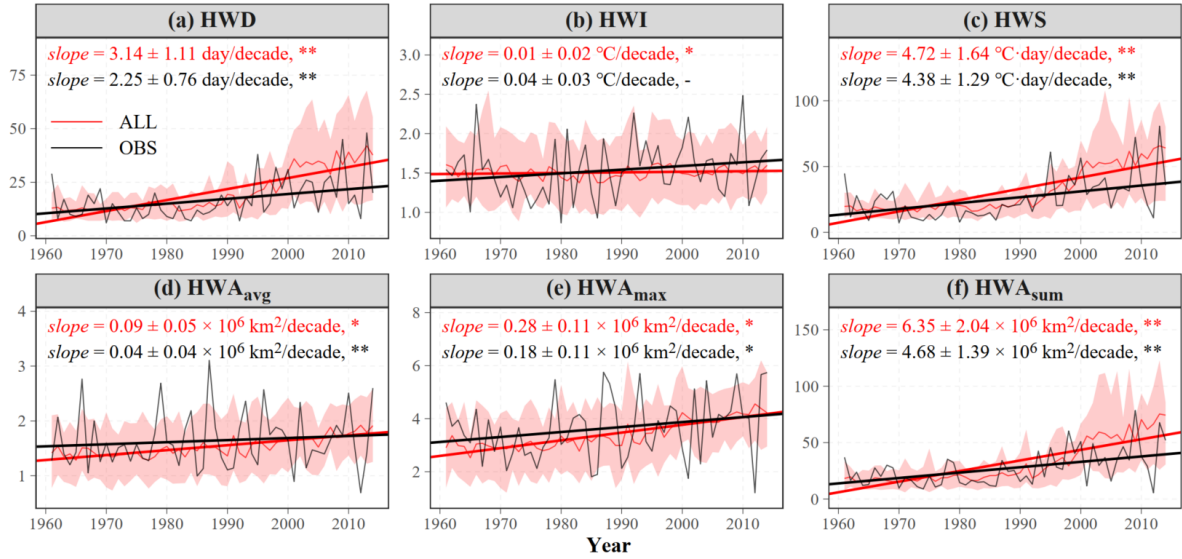


Fig. 3. Annual variation in HI-STHW characteristics in the observations (OBS) and CMIP6 ALL simulations during 1961–2014. HI-STHW characteristics were calculated at the event scale (Table 2). For each year, we only select the annual strongest event, indicated by the largest HWS_{sum} . The red shading represents the 10%–90% interval of CMIP6 GCMs. The thin black and red lines represent the HI-STHW characteristics of the OBS and CMIP6 multimodel ensemble means, respectively. The thick lines represent the linear trend estimated by Sen’s slope. The values of the trends are labeled at the top of each subplot. The symbols “*” and “**” indicate slopes that are significant at the 0.05 and 0.01 levels, respectively, while “-” represents slopes that are nonsignificant. Slope uncertainties (the value after the symbol “ \pm ”) are estimated as the standard deviation of 1,000 bootstrapping samplings for OBS and the standard deviation among CMIP6 GCMs for ALL. The bootstrapping slope uncertainty is calculated by the *slope_boot* function of the *R* package *rtrend* (Kong & Song, 2022).

Fig. 3 shows the annual variation in the characteristics of the annual strongest HI-STHW event based on the observations (OBS) and CMIP6 ALL simulations from 1961 to 2014. For the observed HI-STHWs, we find that the annual HWD, HWS, HWA_{avg} , HWA_{max} and HWA_{sum} increase significantly, with values of 2.25 ± 0.76 days/decade, 4.38 ± 1.29 °C·day/decade, $(0.04 \pm 0.04) \times 10^6$ km²/decade, $(0.18 \pm 0.11) \times 10^6$ km²/decade and $(4.68 \pm 1.39) \times 10^6$ km²/decade, respectively. Although the climate is warming, the HWI remained relatively stable during 1961–2014. Because the expanded area and extended duration of HI-STHW dilute the potential intensification of the HWI (Perkins-Kirkpatrick & Lewis, 2020). For the historical period (1961–1990), HWD, HWS, HWA_{avg} , HWA_{max} and HWA_{sum} have mean values of 12.4 days, 17.7 °C·day, 1.61×10^6 km², 3.43×10^6 km², and 19.30×10^6 km² per year, respectively. For the

recent period (1991–2014), these values are approximately 1.77, 2.0, 1.05, 1.14, and 1.89 times those of the historical period. Compared with CMIP6 simulations without the QMD bias correction (Fig. S7), the magnitude and trends of HI-STHW characteristics of the bias-corrected improved significantly. For the annual characteristics of CMIP6 ALL-simulated HI-STHWs, they match well with those of the observed in magnitudes and trends (Fig. 3). Although CMIP6 ALL-simulated HWD and HWA_{sum} are slightly overestimated after 2000, their 10%-90% intervals cover the observed.

Fig. 4 further compares the spatial pattern of trends in HI-STHW characteristics in the observed and CMIP6 ALL simulations from 1961 to 2014. Because Fig. 4 mainly focuses on the spatial pattern of HI-STHW characteristics, the characteristics are calculated at the grid scale (Table 2). For the observed HI-STHW spatial characteristics, there are widespread increasing trends for HWD, HWF, HWI, and HWS, with mean spatial trend values of 3.26 ± 1.20 days/decade, 0.31 ± 0.15 times/decade, $5.17 \pm 1/78$ °C/decade and 0.93 ± 0.46 °C·day/decade, respectively. For the CMIP6 ALL-simulated HI-STHWs, their trends are very close to that of the observed, being 4.28 ± 1.24 days/decade, 0.29 ± 0.05 times/decade, 5.90 ± 1.00 °C/decade and 1.15 ± 0.37 °C·day/decade in the same order. Different CMIP6 models show good trend consistency (Figs. S8-S11). Despite some differences in spatial distribution patterns of HWI in East China (Fig. 4, c1-c2), the CMIP6 ALL simulations successfully capture the increasing trends in most regions of China for all spatial characteristic indexes (Fig. 4).

The consistency results of Figs. 2-4 confirm that CMIP6 GCMs can capture and reoccur the observed spatiotemporal characteristics of HI-STHW events, and give us confidence in the following detection and attribution analysis, and future evolution of HI-STHW characteristics under different future warming levels.

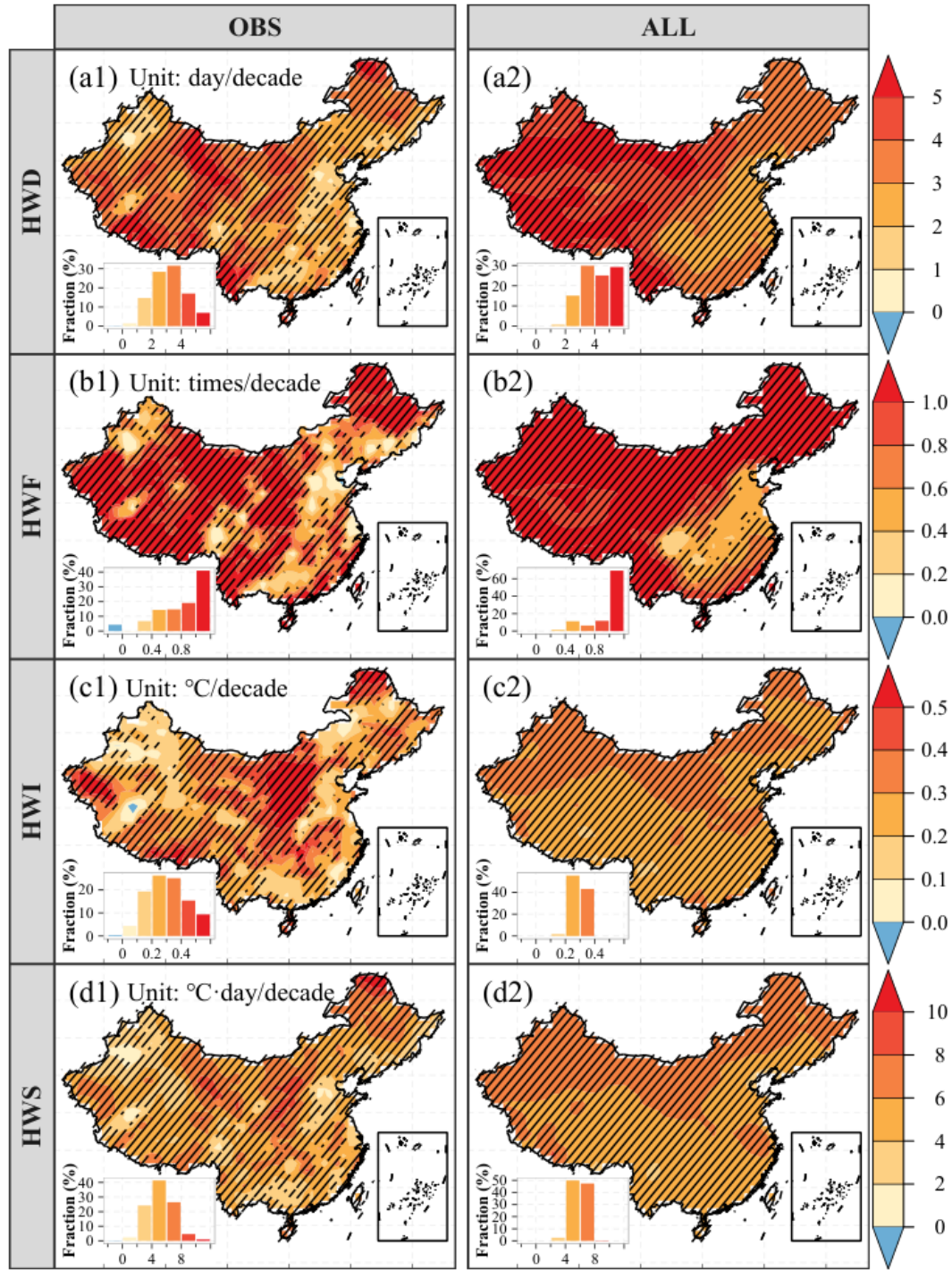
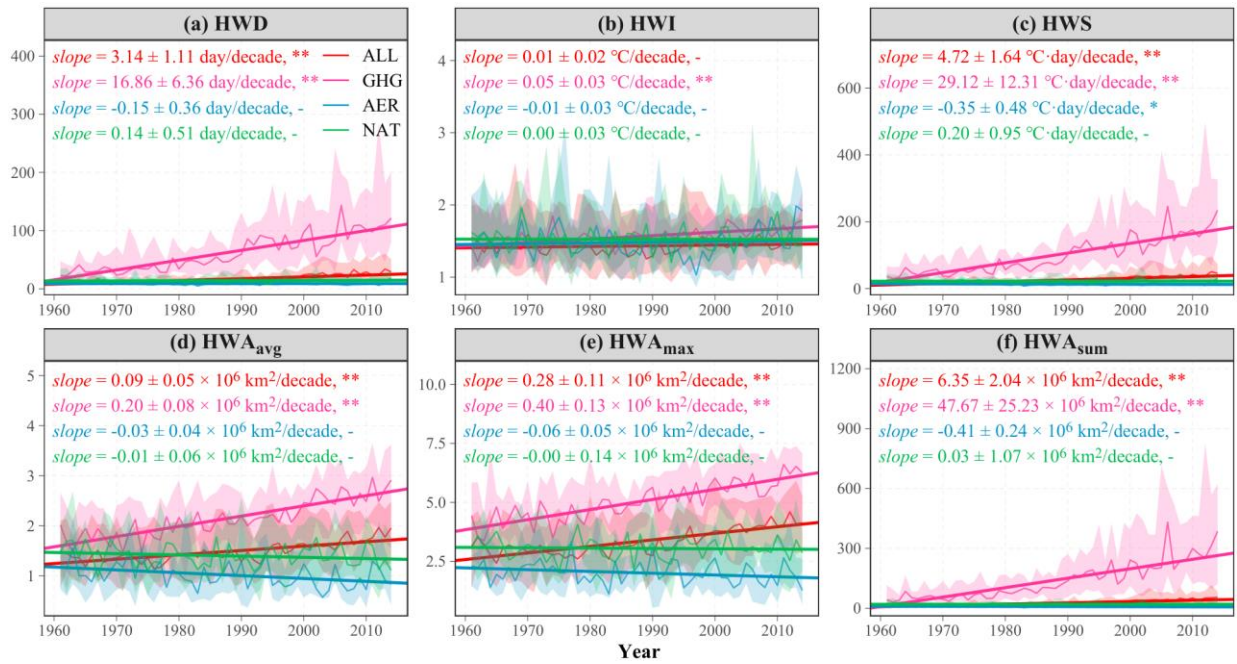


Fig. 4. Trends in HI-STHW characteristics of the observed (left panel) and CMIP6 ALL-simulated (right panel) events during 1961–2014. The duration (HWD), frequency (HWF), intensity (HWI), and severity (HWS) of HI-STHWs are summarized for each grid and each year to show the spatial distribution information of HI-STHW events (see Table 2 and Section 2.3 HI-STHW characteristics at the grid scale for details). All identified HI-STHW events are included here to produce the spatial characteristics. Trends are calculated by Sen’s slope (Kong & Song, 2022; Sen, 1968) method with the help of *R* package *rtrend* (Kong & Song, 2022). For OBS, regions covered by diagonal lines indicate that trends are significant at the 0.05 level; for ALL, it indicates that more than 70% of GCMs share the same trend direction. The trend’s frequency distribution is also shown in the lower-left corner for each subplot.

409

410 **3.2 Detection and Attribution**



411

412 **Fig. 5.** Annual variation in HI-STHW characteristics under different CMIP6 scenarios (ALL, GHG, AER, and
413 NAT) during 1961–2014. Same as Fig. 3, for each year, we only select the annual strongest HI-STHW event.

414

415 Fig. 5 shows the annual variation in HI-STHW characteristics under different CMIP6
416 scenarios. Under the GHG and ALL scenarios, all indexes except HWI have a significant positive
417 trend. Under the AER scenario, the trends become significantly negative. While under the NAT
418 scenario, the trends of all indexes are nonsignificant. Those results indicate that GHG (AER)
419 might have a positive (negative) contribution to the increase of HI-STHW characteristics.
420 Meanwhile, the influence of NAT is ignorable. On the other aspect, we notice that although QMD
421 bias correction has been applied and ALL matches well with OBS for all indexes (Figs. 3 and 4),
422 HI-STHW characteristics are increasing dramatically under the GHG scenario, whose
423 magnitudes are many times of ALL. This implies that HI-STHW characteristics will increase
dramatically under the future warming climate.

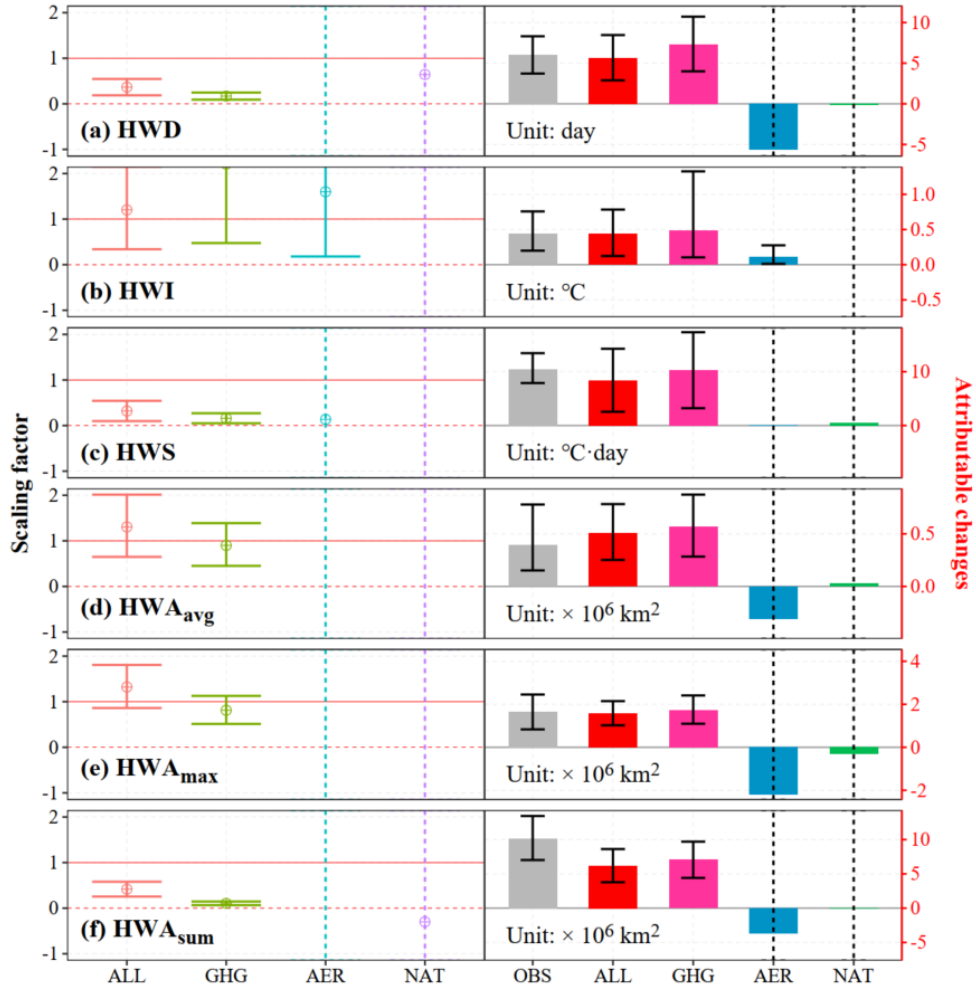


Fig. 6. Scaling factor (left) and attributable changes (right) of ALL, GHG, AER, and NAT for the annual strongest HI-STHW indexes during 1961–2014. Attributable changes are calculated using Eq. 8. The error bars are the 90% uncertain intervals of scaling factor (left) and attributable changes (right). Vertical dashed lines indicate unbounded confidence intervals, and the corresponding scaling factors are nonsignificant. We show only the mean values of their scaling factor and attributable changes in the plot for anthropogenic forcings with an unbounded confidence interval.

We attributed the increases in HI-STHWs to anthropogenic forcings (i.e., ALL, GHG, AER, and NAT) using the ROF optimal fingerprint method. The left panel of Fig.6 shows the best estimate of the one-signal scaling factor and their 90% confidence interval for the annual strongest HI-STHW during 1961–2014. Results show that the signal of ALL and GHG can be significantly detected for all HI-STHW indexes, while the signal of AER and NAT are nonsignificant for all indexes except AER in HWI. For ALL and GHG, their scaling factor's 90% intervals are above zero, which is a sign of significance. Meanwhile, we noticed that the scaling factor of GHG is much smaller than one, which indicates the values of HI-STHW indexes are

overestimated under the GHG scenario. The degree of overestimation under the GHG scenario is significantly higher than that of ALL scenario (Figs. 5 and 6), indicating that values of HI-STHW indexes will grow dramatically in the future warming climate, which is consistent with the results of Fig. 5, and is verified in Figs. 7-9.

The right panel of Fig. 6 shows the attributable changes of HI-STHW indexes during 1961–2014 to ALL, GHG, AER, and NAT. Results show that the ALL simulated changes during the 1961–2014 are 5.7 [2.9, 8.5] days (with the 90% confidence interval in “[]”), 0.44 [0.12, 0.78] °C, 8.39 [2.57, 14.26] °C·day, 0.51 [0.25, 0.78] $\times 10^6 km^2$, 1.57 [1.02, 2.15] $\times 10^6 km^2$, 6.19 [3.78, 8.62] $\times 10^6 km^2$ for HWD, HWI, HWS, HWA_{avg} , HWA_{max} , and HWA_{sum} , respectively. Of which, GHG explains about 130%, 109%, 122%, 112%, 111%, and 114% for the same indexes in the same order. The reason for attributable changes to GHG exceeding 100%, is that AER might have a negative contribution (Fig. 5). The above results indicate GHG dominates the changes of HI-STHW indexes. Although AER might have a negative effect, but can’t be significantly detected. Meanwhile, the attributable changes to NAT are tiny, nonsignificant, and ignorable (Fig. 6).

3.3 Future evolution of HI-STHW events

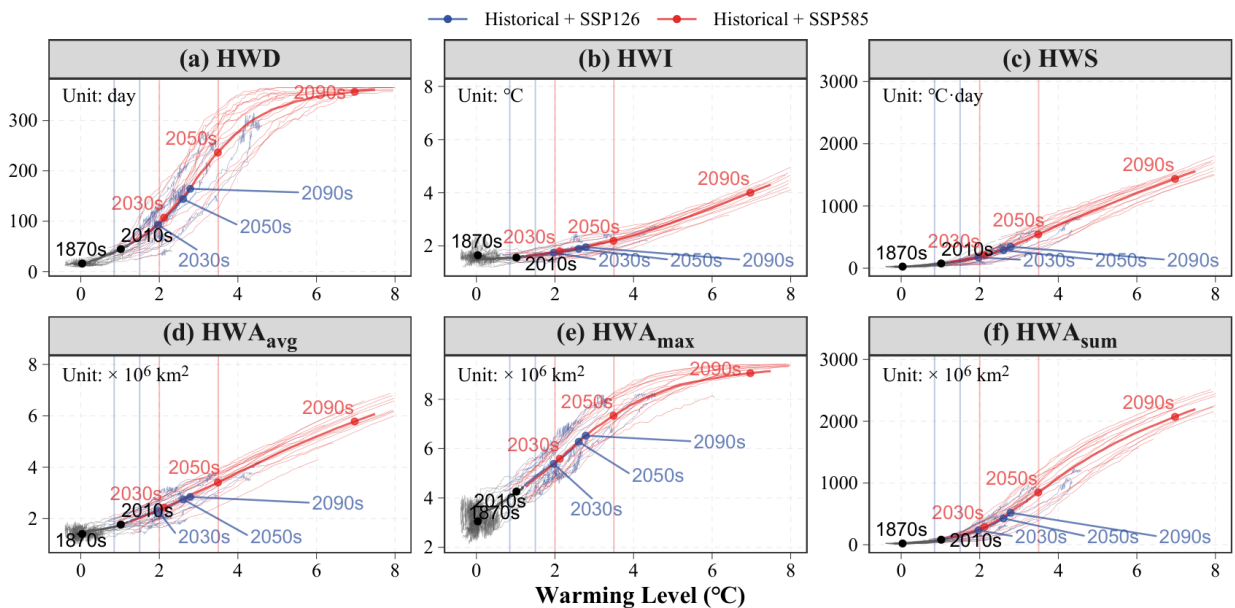


Fig. 7. Simulated changes in HI-STHW characteristics under different warming levels for the annual strongest

HI-STHW event. The warming level refers to the rise of HI_{max} with respect to preindustrial period. It was calculated individually for each GCM by subtracting the China area-weighted annual mean HI_{max} from the averaged value during 1861–1880. Both warming levels and HI-STHW characteristics are smoothed by a 21-year moving window. The thinner lines represent projections of each GCM, while the thicker lines represent the projection of the multimodel ensemble means. Black lines are models of the historical ALL scenario. The blue and red lines are the SSP126 and SSP585 scenarios, respectively. The four vertical thinner lines indicate warming levels of 0.85 °C, 1.5 °C, 2.0 °C, and 3.5 °C.

SSPs are CMIP6 future scenarios under different climate policies and different levels of anthropogenic GHG emissions, with CO₂ concentrations ranging from 393 to 1135 ppm by 2100 for the lowest and highest emission scenarios (Meinshausen et al., 2020). As GHG is primarily responsible for the increase of HI-STHW indexes, we further present the HI-STHW characteristics under two representative GHG emission pathways during 2015–2100, namely, SSP126 and SSP585 (Fig. 7). With the increase in warming, the HI-STHW characteristics increase consistently and dramatically. Such an increase is independent of the development paths, as indicated by the overlapping lines between the SSP126 and SSP585 scenarios in Fig. 7. This is consistent with previous HW studies at the grid scale (Frölicher et al., 2018b; Kong et al., 2020). These results indicate that even though GCMs might overestimate or underestimate warming levels, they influence only the time required to reach the warming level but will not alter the HI-STHW characteristics at a certain warming level. This gives us more confidence in the robustness of our results.

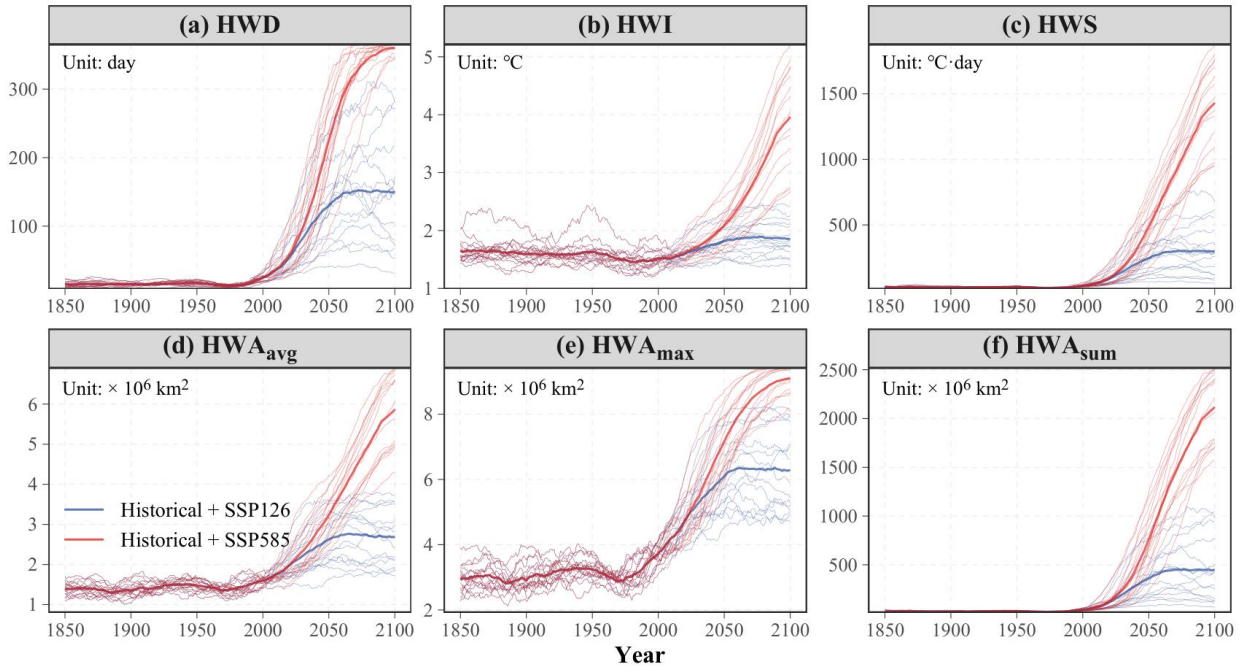


Fig. 8. Temporal evolution of the annual strongest HI-STHWs' characteristics during 1851–2100.

Although independent of the development path, the difference between SSP1-2.6 and SSP5-8.5 is noticeable after the 2050s (Fig. 8). Under the SSP585 scenario, after the 2050s, the rate of increase in HI-STHW characteristics dramatically accelerates. By 2100, the warming level is projected to be 7.2 [4.9, 8.9] °C. At that time, the annual most severe HI-STHW event will last almost the whole year, and influence 96% regions of China on the most serious day, with HWD, HWA_{max} , HWA_{sum} about 358.2 [340.4, 365.2] days, 9.11 [8.51, 9.41] $\times 10^6$ km² and 2137.1 [1576.9, 2580.4] $\times 10^6$ km², respectively. At that time, HWD and HWA_{sum} are about 24.5 [17.2, 31.6] and 107.2 [70, 129.9] times the preindustrial period. Under the SSP126 scenario, the human-perceived temperature warming level exceeds 1.5 °C in the 2030s and 2.5 °C in the 2050s and stabilizes thereafter. Under this scenario, the HI-STHW characteristics peak in the 2050s. Even under the SSP126 scenario, the warming level still can reach 2.69 [1.78, 4.29] °C by 2100. At that time, HWD and HWA_{sum} are 157.2 [53.9, 273.5] days and 493.05 [102.78, 978.65] $\times 10^6$ km², which are about 10.8 and 26.1 times the preindustrial period. When the warming level is reduced by 0.5 °C, the magnitude of HWA_{sum} will approximately decrease by half. If warming could be limited to 2.0 and 1.5 °C, HWA_{sum} can be reduced to 1/2 and 1/4 of the level of SSP126

by 2100 (Fig. 7). Those results indicate that in the future climate warming climate, HI-STHW indexes are projected to escalate approximately in an exponential manner. Implementing effective strategies to curb temperature rise could substantially mitigate the adverse impacts of HI-STHW events.

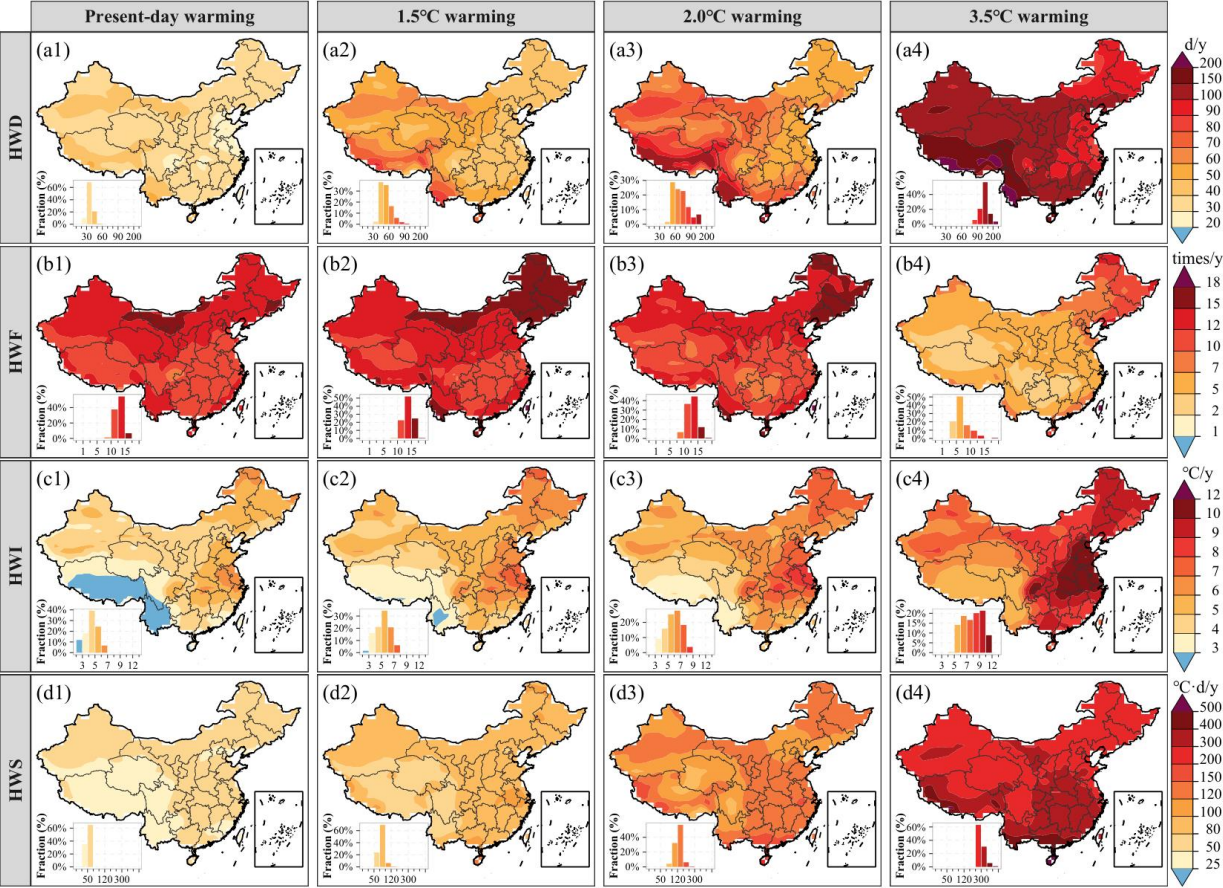


Fig. 9. Spatial distribution of HI-STHW characteristics under different warming levels.

The response of HI-STHW characteristics to anthropogenic warming varies spatially. Fig. 9 shows the spatial distribution of HI-STHW characteristics under different warming levels. In general, the HWD, HWI, and HWS increase consistently with increasing warming levels, while the HWF presents a decreasing trend. This is mainly because short-duration events are merged into long-duration events and hence decrease the HWF. Under the 3.5°C warming level, in Tibet and Yunnan, a high HWD is observed, whereas North China Plain exhibits the highest HWI, reaching up to 10°C. Meanwhile, South China, encompassing Tibet and Yunnan, displays a strong HWS. Specifically, while Tibet has a lower HWI compared to eastern regions, it

compensates with an extended HWD, culminating in an HWS severity level commensurate with that in Yunnan and Guangdong provinces. Inconsistencies in the monthly temperature rise throughout the year can disrupt the temporal continuity of HI-STHW events (Song et al., 2022, their Fig. 4 and Fig. 8). We guess that consistent monthly temperature rise is the reason for the higher HWD in Tibet. In the South China provinces, notably Guangdong, both high HWD and HWI are present; their duration and intensity are second only to Tibet and North China Plain, respectively, resulting in a higher HWS. North China Plain has the highest HWI in China, reaching up to 10°C under a 3.5°C warming scenario, which aligns with a previous study by (Kang & Eltahir, 2018). However, its shorter duration (HWD) results in a lower HWS compared to South China and Tibet. This region necessitates heightened vigilance for short-duration extreme HI-STHW events.

4. Discussion

4.1 Comparison with previous STHW studies

Luo et al. (2022a) also studied the change pattern of STHW events in China using a similar spatiotemporal clustering technique. But their STHW events mainly focused on air temperature T_{max} based STHW. In our study, the trends of HWD, HWA_{max} and HWA_{sum} during 1961–2014 are 2.25 ± 0.76 day/decade, $(0.18 \pm 0.11) \times 10^6$ km²/decade and $(4.68 \pm 1.39) \times 10^6$ km²/decade, respectively. The values of HWD and HWA_{sum} are larger than those of (Luo et al., 2022a), who obtained values of 1.14 day/decade and 1.30×10^6 km²/decade, respectively. This can be attributed to the following reasons: (1) The difference in the research period and selected STHW events: Luo et al. (2022a) focused only on the summer, and selected all STHW events only if their HWD ≥ 3 days and $HWA_{max} \geq 1$ million km². While we considered the whole year, and mainly focused on the annual most severe HI-STHW events, which produces longer HWD and HWA_{sum} . (2) The faster increasing speed in HI_{max} (J. Li et al., 2018; Song et al., 2022): We used HI_{max}

to define STHWs, while (Luo et al., 2022a) used T_{max} . The increasing trend of HI_{max} is stronger than that of T_{max} in 62.4% of the regions of China (Fig. S12c), and the China area-weighted HI_{max} increased at a rate of 0.023°C/decade faster than T_{max} during 1961–2014 (Fig. S12d). Despite these differences, the trend of HWA_{max} is similar to that of (Luo et al., 2022a), which confirms that the detection of HI-STHW events is correct. Meanwhile, a significant positive increasing trend is found for HWD, and HWA_{sum} in both the study by (Luo et al., 2022a) and our study, indicating that the increasing pattern of the HI-STHW is robust.

4.2 The reasons for the intensification of HI-STHW

We found that GHG-induced anthropogenic warming dominates the increases of HI-STHW characteristics. This is consistent with the result of (Vogel et al., 2020). They also found that the increasing pattern of STHW is mainly attributed to climate warming. When using a time-varying threshold, which considers the effect of climate warming, to identify HW grids, the increasing pattern of STHW will disappear. However, the spatial pattern of STHW characteristics can't be fully explained by climate warming alone. The asymmetric warming across different months explains the regional difference in the HI-STHW characteristics under a certain warming level and explains why the severity of HI-STHW in Tibet is more serious than in North China Plain and South China in the future 3.5°C warming climate.

Additionally, from the perspective of synoptics and atmospheric circulation, the Western North Pacific Subtropical High (WNPSH) is another factor responsible for the increase of HI-STHW in China (N. Li et al., 2021; Q. Liu et al., 2019). The stronger westward WNPSH usually corresponds to the long-lived HWs (N. Li et al., 2021). Under the control of WNPSH, there is prevailing sinking, dry, and warm air, which is favorable to the formation and maintenance of HW, as well as the HI-STHW. Under the warming climate, NPSH will be further intensified with stronger subsidence motion and larger subsidence area (W. Li et al., 2012; Yang et al., 2022), which corresponds to the longer-lasting and more serious HI-STHW. Other studies also argued

that large-scale circulation indexes, e.g., El Niño-Southern Oscillation (ENSO), and North Atlantic Oscillation (NAO), could also explain the changes in STHW (Luo et al., 2022b). However, this is not supported in our study. When regressed HI-STHW characteristic indexes to ENSO or NAO, the regression coefficients are nonsignificant, which implies ENSO and NAO contribute little to the increases of HI-STHW on the annual scale.

5. Conclusion

HI-STHWs became longer lasting and larger during 1961–2014. In the historical period (1961–1990), the HWD, HWS, HWA_{avg} , HWA_{max} and HWA_{sum} have mean values of 12.4 days, 17.7 °C·day, 1.61×10^6 km², 3.43×10^6 km², and 19.30×10^6 km² per year, respectively. In the recent period (1991–2014), these values are approximately 1.77, 2.0, 1.05, 1.14, and 1.89 times those of the historical period. For the annual variation and spatial changing pattern of HI-STHW characteristic indexes, the bias-corrected CMIP6 ALL simulations match well with the observed. This indicates CMIP6 GCMs can capture and reoccur the changing pattern of HI-STHWs, and provide reliable results in the historical attribution analysis and future evolution analysis.

In the attribution analysis, we attributed the increases in HI-STHWs to anthropogenic forcings (i.e., ALL, GHG, AER, and NAT) using the ROF optimal fingerprint method. For all HI-STHW indexes except HWI, the GHG signal is significantly detected, while the AER and NAT signals are not. GHG is the primary factor contributing to the increases in HI-STHWs. For HWD, HWS, HWS_{avg} , HWS_{max} , and HWA_{sum} , GHG alone explains about 130%, 122%, 112%, 111% and 114%. Although nonsignificant, AER should have a negative contribution to the increases of those indexes. As the increases in HI-STHWs are mainly attributed to anthropogenic GHG, we further present the future evolution of HI-STHWs under two different GHG emissions scenarios (i.e., SSP126 and SSP585). The pattern of increases in the HI-STHW characteristics is

determined by the warming level and is independent of the development path. Under the SSP585 scenario, the warming level of HI_{max} is projected to be 7.2 [4.9, 8.9] °C by 2100 in China. At that time, the annual most severe HI-STHW event will last almost the whole year, and influence 96% regions of China on the most serious day. Meanwhile, HWD and HWA_{sum} are 24.5 [17.2, 31.6] and 107.2 [70, 129.9] times the preindustrial period. However, if the warming level could be limited to 2/1.5 °C, HWD and HWA_{sum} would be 3.4/5.4 and 8.2/16.2 times smaller than that under the SSP585 scenario by 2100. Additionally, the response of HI-STHWs to human-induced warming varies spatially. Tibet and South China are expected to experience more severe HI-STHWs, while the North China Plain should be vigilant against high-intensity and short-duration HI-STHW events.

Author contributions

D.K. and X.G. designed this study. D.K., Y.X., and H.S. performed the data analysis. D.K. wrote the first draft. All authors contributed to the writing and reviewing of the article. The authors declare that they have no competing interests.

Acknowledgments

This study was supported by the China National Key R&D Program (Grant 2023YFE0103900), the National Natural Science Foundation of China (Grants 42101052), the Natural Science Foundation of Hubei Province (Grant 2021CFB198), the Natural Science Foundation of the Jiangsu Higher Education Institutions of China (Grant 20KJB170016), and the Fundamental Research Funds for the Central Universities, China University of Geosciences (Wuhan) (Grant CUG2106107). We acknowledge the World Climate Research Programme's Working Group, which provided the CMIP6 simulations. We acknowledge Wu Jia, who provided us with the

observed temperature dataset CN05.1. We also acknowledge the editor Filippo Giorgi and the two anonymous reviewers.

Data Availability Statement

All data used to generate figures in the main text are available at zenodo (Kong, 2023).

References

- Allen, M. R., & Stott, P. A. (2003). Estimating signal amplitudes in optimal fingerprinting, part I: Theory. *Climate Dynamics*, 21(5–6), 477–491. <https://doi.org/10.1007/s00382-003-0313-9>
- Allen, M. R., & Tett, S. F. B. (1999). Checking for model consistency in optimal fingerprinting. *Climate Dynamics*, 15(6), 419–434. <https://doi.org/10.1007/s003820050291>
- Bezanson, J., Edelman, A., Karpinski, S., & Shah, V. B. (2017). Julia: A fresh approach to numerical computing. *SIAM Review*, 59(1), 65–98. Retrieved from <https://doi.org/10.1137/141000671>
- Chen, H., & Sun, J. (2017). Contribution of human influence to increased daily precipitation extremes over China. *Geophysical Research Letters*, 44(5), 2436–2444. <https://doi.org/10.1002/2016GL072439>
- Christidis, N., Jones, G. S., & Stott, P. A. (2015). Dramatically increasing chance of extremely hot summers since the 2003 European heatwave. *Nature Climate Change*, 5(1), 46–50. <https://doi.org/10.1038/nclimate2468>
- Dunne, J. P., Stouffer, R. J., & John, J. G. (2013). Reductions in labour capacity from heat stress under climate warming. *Nature Climate Change*, 3(6), 563–566. <https://doi.org/10.1038/nclimate1827>
- Fischer, E. M., & Knutti, R. (2013). Robust projections of combined humidity and temperature extremes. *Nature Climate Change*, 3(2), 126–130. <https://doi.org/10.1038/nclimate1682>
- Frölicher, T. L., Fischer, E. M., & Gruber, N. (2018a). Marine heatwaves under global warming. *Nature*, 560(7718), 360–364. <https://doi.org/10.1038/s41586-018-0383-9>
- Frölicher, T. L., Fischer, E. M., & Gruber, N. (2018b). Marine heatwaves under global warming. *Nature*, 560(7718), 360–364. <https://doi.org/10.1038/s41586-018-0383-9>
- Gu, X., Zhang, Q., Li, J., Singh, V. P., Liu, J., Sun, P., & Cheng, C. (2019). Attribution of Global Soil Moisture Drying to Human Activities: A Quantitative Viewpoint. *Geophysical Research Letters*, 46(5), 2573–2582. <https://doi.org/10.1029/2018GL080768>
- Kang, S., & Eltahir, E. A. B. (2018). North China Plain threatened by deadly heatwaves due to climate change and irrigation. *Nature Communications*, 9(1), 1–9. <https://doi.org/10.1038/s41467-018-05252-y>
- Keellings, D., & Moradkhani, H. (2020). Spatiotemporal Evolution of Heat Wave Severity and Coverage Across the United States. *Geophysical Research Letters*, 47(9), 1–9. <https://doi.org/10.1029/2020GL087097>
- Kim, Y. H., Min, S. K., Zhang, X., Zwiers, F., Alexander, L. V., Donat, M. G., & Tung, Y. S. (2016). Attribution of extreme temperature changes during 1951–2010. *Climate Dynamics*, 46(5–6), 1769–1782. <https://doi.org/10.1007/s00382-015-2674-2>

- Kirchmeier-Young, M. C., & Zhang, X. (2020). Human influence has intensified extreme precipitation in North America. *Proceedings of the National Academy of Sciences of the United States of America*, 117(24), 13308–13313. <https://doi.org/10.1073/pnas.1921628117>
- Kirchmeier-Young, M. C., Zwiers, F. W., & Gillett, N. P. (2017). Attribution of extreme events in Arctic Sea ice extent. *Journal of Climate*, 30(2), 553–571. <https://doi.org/10.1175/JCLI-D-16-0412.1>
- Kong, D., & Song, H. (2022). rtrend: Trend Estimating Tools. Retrieved from <https://cran.r-project.org/package=rtrend>
- Kong, D., Gu, X., Li, J., Ren, G., & Liu, J. (2020). Contributions of Global Warming and Urbanization to the Intensification of Human-Perceived Heatwaves Over China. *Journal of Geophysical Research: Atmospheres*, 125(18), 0–2. <https://doi.org/10.1029/2019JD032175>
- Kong D. (2023). Data of "Contribution of Anthropogenic Activities to the Intensification of Heat Index-based Spatiotemporally Contiguous Heatwave Events in China" (v2.0). Zenodo. <https://doi.org/10.5281/zenodo.10360695>
- Larcom, S., She, P. W., & van Gevelt, T. (2019). The UK summer heatwave of 2018 and public concern over energy security. *Nature Climate Change*, 9(5), 370–373. <https://doi.org/10.1038/s41558-019-0460-6>
- Li, C., Sun, Y., Zwiers, F., Wang, D., Zhang, X., Chen, G., & Wu, H. (2020). Rapid Warming in Summer Wet Bulb Globe Temperature in China with Human-Induced Climate Change. *Journal of Climate*, 33(13), 5697–5711. <https://doi.org/10.1175/jcli-d-19-0492.1>
- Li, J., Chen, Y. D., Gan, T. Y., & Lau, N.-C. (2018). Elevated increases in human-perceived temperature under climate warming. *Nature Climate Change*, 8(1), 43–47. <https://doi.org/10.1038/s41558-017-0036-2>
- Li, N., Xiao, Z., & Zhao, L. (2021). A recent increase in long-lived heatwaves in China under the joint influence of south Asia and western north pacific subtropical highs. *Journal of Climate*, 34(17), 7167–7179. <https://doi.org/10.1175/JCLI-D-21-0014.1>
- Li, W., Li, L., Ting, M., & Liu, Y. (2012). Intensification of Northern Hemisphere subtropical highs in a warming climate. *Nature Geoscience*, 5(11), 830–834. <https://doi.org/10.1038/ngeo1590>
- Li, Y., Chen, K., Yan, J., & Zhang, X. (2021). Uncertainty in optimal fingerprinting is underestimated. *Environmental Research Letters*, 16(8). <https://doi.org/10.1088/1748-9326/ac14ee>
- Li, Z., Yan, Z., Zhu, Y., Freychet, N., & Tett, S. (2020). Homogenized Daily Relative Humidity Series in China during 1960–2017. *Advances in Atmospheric Sciences*, 37(4), 318–327. <https://doi.org/10.1007/s00376-020-9180-0>
- Liu, J., Zhang, J., Kong, D., Feng, X., Feng, S., & Xiao, M. (2021). Contributions of Anthropogenic Forcings to Evapotranspiration Changes Over 1980–2020 Using GLEAM and CMIP6 Simulations. *Journal of Geophysical Research: Atmospheres*, 126(22), 1–14. <https://doi.org/10.1029/2021JD035367>
- Liu, Q., Zhou, T., Mao, H., & Fu, C. (2019). Decadal variations in the relationship between the western Pacific subtropical high and summer heat waves in east China. *Journal of Climate*, 32(5), 1627–1640. <https://doi.org/10.1175/JCLI-D-18-0093.1>
- Lo, S. H., Chen, C. T., Russo, S., Huang, W. R., & Shih, M. F. (2021). Tracking heatwave extremes from an event perspective. *Weather and Climate Extremes*, 34, 100371. <https://doi.org/10.1016/j.wace.2021.100371>
- Luo, M., & Lau, N.-C. C. (2018). Increasing heat stress in urban areas of eastern China: Acceleration by urbanization. *Geophysical Research Letters*, 45(23), 13,060–13,069. <https://doi.org/10.1029/2018GL080306>

- Luo, M., Lau, N., Liu, Z., Wu, S., Wang, X., Lau, G., et al. (2022a). An observational investigation of spatiotemporally contiguous heatwaves in China from a 3D perspective. *Geophysical Research Letters*, 49(6), 1–10. <https://doi.org/10.1029/2022gl097714>
- Luo, M., Wang, X., Dong, N., Zhang, W., Li, J., Wu, S., et al. (2022b). Two different propagation patterns of spatiotemporally contiguous heatwaves in China. *Npj Climate and Atmospheric Science*, 5(1). <https://doi.org/10.1038/s41612-022-00313-y>
- Lyon, B., Barnston, A. G., Coffel, E., & Horton, R. M. (2019). Projected increase in the spatial extent of contiguous US summer heat waves and associated attributes. *Environmental Research Letters*, 14(11). <https://doi.org/10.1088/1748-9326/ab4b41>
- Ma, F., Yuan, X., & Li, H. (2022). Characteristics and circulation patterns for wet and dry compound day-night heat waves in mid-eastern China. *Global and Planetary Change*, 213(May), 103839. <https://doi.org/10.1016/j.gloplacha.2022.103839>
- Ma, S., Zhou, T., Stone, D. A., Angélil, O., & Shiogama, H. (2017). Attribution of the July–August 2013 heat event in Central and Eastern China to anthropogenic greenhouse gas emissions. *Environmental Research Letters*, 12(5). <https://doi.org/10.1088/1748-9326/aa69d2>
- McMichael, A. J., Woodruff, R. E., & Hales, S. (2006). Climate change and human health: Present and future risks. *Lancet*, 367(9513), 859–869. [https://doi.org/10.1016/S0140-6736\(06\)68079-3](https://doi.org/10.1016/S0140-6736(06)68079-3)
- Meinshausen, M., Nicholls, Z. R. J., Lewis, J., Gidden, M. J., Vogel, E., Freund, M., et al. (2020). The shared socio-economic pathway (SSP) greenhouse gas concentrations and their extensions to 2500. *Geoscientific Model Development*, 13(8), 3571–3605. <https://doi.org/10.5194/gmd-13-3571-2020>
- Mora, C., Dousset, B., Caldwell, I. R., Powell, F. E., Geronimo, R. C., Bielecki, C. R., et al. (2017). Global risk of deadly heat. *Nature Climate Change*, 7(7), 501–506. <https://doi.org/10.1038/nclimate3322>
- Perkins-Kirkpatrick, S. E., & Lewis, S. C. (2020). Increasing trends in regional heatwaves. *Nature Communications*, 11(1), 1–8. <https://doi.org/10.1038/s41467-020-16970-7>
- Perkins, S. E. (2015). A review on the scientific understanding of heatwaves-Their measurement, driving mechanisms, and changes at the global scale. *Atmospheric Research*, 164–165, 242–267. <https://doi.org/10.1016/j.atmosres.2015.05.014>
- Ribes, A., & Terray, L. (2013). Application of regularised optimal fingerprinting to attribution. Part II: Application to global near-surface temperature. *Climate Dynamics*, 41(11–12), 2837–2853. <https://doi.org/10.1007/s00382-013-1736-6>
- Ribes, A., Planton, S., & Terray, L. (2013). Application of regularised optimal fingerprinting to attribution. Part I: method, properties and idealised analysis. *Climate Dynamics*, 41(11–12), 2817–2836. <https://doi.org/10.1007/s00382-013-1735-7>
- Rothfusz, L. P., & Headquarters, N. S. R. W. S. S. R. (1990). The heat index equation (or, more than you ever wanted to know about heat index). *Fort Worth, Texas: National Oceanic and Atmospheric Administration, National Weather Service, Office of Meteorology*, 9023, 23–90. Retrieved from papers://c6bd9143-3623-4d4f-963f-62942ed32f11/Paper/p395
- Russo, S., Sillmann, J., & Sterl, A. (2017). Humid heat waves at different warming levels. *Scientific Reports*, 7(1), 1–7. <https://doi.org/10.1038/s41598-017-07536-7>
- Samaniego, L., Thober, S., Kumar, R., Wanders, N., Rakovec, O., Pan, M., et al. (2018). Anthropogenic warming exacerbates European soil moisture droughts. *Nature Climate Change*, 8(5), 421–426. <https://doi.org/10.1038/s41558-018-0138-5>
- Samaniego, Luis, Kumar, R., & Zink, M. (2013). Implications of parameter uncertainty on soil moisture drought analysis in Germany. *Journal of Hydrometeorology*, 14(1), 47–68. <https://doi.org/10.1175/JHM-D-12-075.1>
- Sen, P. K. (1968). Estimates of the Regression Coefficient Based on Kendall’s Tau. *Journal of the American Statistical Association*, 63(324), 1379. <https://doi.org/10.2307/2285891>

- Seong, M.-G., Min, S.-K., Kim, Y.-H., Zhang, X., & Sun, Y. (2021). Anthropogenic Greenhouse Gas and Aerosol Contributions to Extreme Temperature Changes during 1951–2015. *Journal of Climate*, 34(3), 857–870. <https://doi.org/10.1175/JCLI-D-19-1023.1>
- Song, H., Kong, D., Xiong, L., Gu, X., & Liu, J. (2022). Inter-Comparison of Diverse Heatwave Definitions in the Analysis of Spatiotemporally Contiguous Heatwave Events over China. *Remote Sensing*, 14(16), 4082. <https://doi.org/10.3390/rs14164082>
- Stott, P. A., Stone, D. A., & Allen, M. R. (2004). Human contribution to the European heatwave of 2003. *Nature*, 432(7017), 610–614. <https://doi.org/10.1038/nature03089>
- Sun, Y., Zhang, X., Zwiers, F. W., Song, L., Wan, H., Hu, T., et al. (2014). Rapid increase in the risk of extreme summer heat in Eastern China. *Nature Climate Change*, 4(12), 1082–1085. <https://doi.org/10.1038/nclimate2410>
- Sun, Y., Song, L., Yin, H., Zhang, X., Stott, P., Zhou, B., & Hu, T. (2016). 20. Human influence on the 2015 extreme high temperature events in Western China. *Bulletin of the American Meteorological Society*, 97(12), S102–S106. <https://doi.org/10.1175/BAMS-D-16-0158.1>
- Sun, Y., Zhang, X., Ren, G., Zwiers, F. W., & Hu, T. (2016). Contribution of urbanization to warming in China. *Nature Climate Change*, 6(7), 706–709. <https://doi.org/10.1038/nclimate2956>
- Vogel, M. M., Zscheischler, J., Fischer, E. M., & Seneviratne, S. I. (2020). Development of Future Heatwaves for Different Hazard Thresholds. *Journal of Geophysical Research: Atmospheres*, 125(9). <https://doi.org/10.1029/2019JD032070>
- Wu, J., & Gao, X. J. (2013). A gridded daily observation dataset over China region and comparison with the other datasets. *Acta Geophysica Sinica*, 56(4), 1102–1111. <https://doi.org/10.6038/cjg20130406>, <https://ccrc.iap.ac.cn/resource/detail?id=228>
- Yang, K., Cai, W., Huang, G., Hu, K., Ng, B., & Wang, G. (2022). Increased variability of the western Pacific subtropical high under greenhouse warming. *Proceedings of the National Academy of Sciences of the United States of America*, 119(23), 1–9. <https://doi.org/10.1073/pnas.2120335119>
- You, Q. L., Jiang, Z. H., Kong, L., Wu, Z. W., Bao, Y. T., Kang, S. C., & Pepin, N. (2017). A comparison of heat wave climatologies and trends in China based on multiple definitions. *Climate Dynamics*, 48(11), 3975–3989. <https://doi.org/10.1007/s00382-016-3315-0>
- Yuan, W., Cai, W., Chen, Y., Liu, S. S. S. S. S. S., Dong, W., Zhang, H., et al. (2016). Severe summer heatwave and drought strongly reduced carbon uptake in Southern China. *Scientific Reports*, 6(January 2015), 1–12. <https://doi.org/10.1038/srep18813>
- Zhang, H., Luo, M., Pei, T., Liu, X., Wang, L., Zhang, W., et al. (2023). Unequal urban heat burdens impede climate justice and equity goals. *Innovation*, 4(5), 100488. <https://doi.org/10.1016/j.xinn.2023.100488>

Supporting Information References

- Cannon, A. J., Sobie, S. R., & Murdock, T. Q. (2015). Bias correction of GCM precipitation by quantile mapping: How well do methods preserve changes in quantiles and extremes? *Journal of Climate*, 28(17), 6938–6959. <https://doi.org/10.1175/JCLI-D-14-00754.1>
- Song, H., Kong, D., Xiong, L., Gu, X., & Liu, J. (2022). Inter-Comparison of Diverse Heatwave Definitions in the Analysis of Spatiotemporally Contiguous Heatwave Events over China. *Remote Sensing*, 14(16), 4082. <https://doi.org/10.3390/rs14164082>